

Robust estimation based nonlinear higher order sliding mode control strategies for PMSG-WECS

Awais NAZIR¹, Safdar Abbas KHAN¹, Malak Adnan KHAN², Zaheer ALAM³, Imran KHAN^{4*},
Muhammad IRFAN⁵, Saifur REHMAN⁵, and Grzegorz NOWAKOWSKI⁶

¹ Department of Electrical Engineering, National University of Science and Technology, Pakistan

² Department of Electronics Engineering, University of Engineering and Technology Peshawar, Abbottabad campus, Pakistan

³ Department of Electrical and Computer Engineering, COMSATS University Islamabad, Abbottabad Campus, Pakistan

⁴ Department of Electrical, Electronics and Computer Systems, College of Engineering and Technology, University of Sargodha, Pakistan

⁵ Electrical Engineering Department, College of Engineering, Najran University, Saudi Arabia

⁶ Faculty of Electrical and Computer Engineering, Cracow University of Technology, Warszawska 24, 31-155 Cracow, Poland

Abstract. The wind energy conversion systems (WECS) suffer from an intermittent nature of source (wind) and the resulting disparity between power generation and electricity demand. Thus, WECS are required to be operated at maximum power point (MPP). This research paper addresses a sophisticated MPP tracking (MPPT) strategy to ensure optimum (maximum) power out of the WECS despite environmental (wind) variations. This study considers a WECS (fixed pitch, 3 KW, variable speed) coupled with a permanent magnet synchronous generator (PMSG) and proposes three sliding mode control (SMC) based MPPT schemes, a conventional first order SMC (FOSMC), an integral back-stepping-based SMC (IBSMC) and a super-twisting reachability-based SMC, for maximizing the power output. However, the efficacy of MPPT/control schemes rely on availability of system parameters especially, uncertain/nonlinear dynamics and aerodynamic terms, which are not commonly accessible in practice. As a remedy, an off-line artificial function-fitting neural network (ANN) based on Levenberg-Marquardt algorithm is employed to enhance the performance and robustness of MPPT/control scheme by effectively imitating the uncertain/nonlinear drift terms in the control input pathways. Furthermore, the speed and missing derivative of a generator shaft are determined using a high-gain observer (HGO). Finally, a comparison is made among the stated strategies subjected to stochastic and deterministic wind speed profiles. Extensive MATLAB/Simulink simulations assess the effectiveness of the suggested approaches.

Key words: WECS; robust control; MPPT; back-stepping; SMC; super-twisting algorithm (STA); high gain observer; ANN; function fitting.

1. INTRODUCTION

Wind, an infinite gift of nature, encompasses a major portion as green energy alternative, opposed to the traditional resources. An obvious environment friendly nature, low operating cost, high energy yield, cost-effectiveness high efficiency accompanied by the recent technological advancements have raised wind energy to a leading resource amongst its competitors. Thus, the wind energy has been covering a major portion of the ever-increasing energy demands [1].

Optimizing the efficiency and hence maximum power output of WECS has been relying on both the system point of operation and wind speed. Thus, an optimal efficiency, from WECS, requires an MPPT scheme to be robust. The MPPT, in relation to the wind speed offered to the wind turbines (WT), has to adjust/regulate the AC generator speed. Research conducted previously, [1, 2], has highlighted the importance of employing an MPPT control scheme to determine the ideal operating point for WECS.

The utilization of wind power through WECS has experienced a significant rise due to the escalating demand for sustainable and clean energy sources around the globe. As a renewable energy technology, WECS have gained popularity among countries and organizations as they harness the power of wind to produce electricity, thus offering a viable solution to meet energy needs while minimizing environmental impact. They are highly versatile and can be used in a range of applications, from small-scale residential installations to large-scale wind farms that can power entire communities.

WTs in WECS may have a fixed or variable speed, depending on the particular system design. In the case of fixed-speed WTs (FSWTs), the generated electricity is directly supplied to the utility grid and is thus referred to as “direct drive” WECS. The generator output of variable speed wind turbines (VSWTs) is sent to the utility grid after being synchronized with the grid frequency and other parameters, as in contrast to other types of generators. Due to the variable shaft speeds of VSWTs, they can harvest the maximum amount of power from any wind speed [3, 4]. In general, a VSWT offers 10–15% increase in energy output over an FSWT, as well as less power fluctuation and mechanical stress [5].

In WECS, the mechanical/kinetic energy, captured by WTs, is utilized by an AC generator to produce electricity for domes-

*e-mail: imran.khan@uos.edu.pk

Manuscript submitted 2023-03-20, revised 2023-07-25, initially accepted for publication 2023-08-13, published in October 2023.

tic and commercial purposes. There are three common types of these generators, a doubly-fed induction generator (DFIG), a field-excited synchronous generator (FESG) and a permanent magnet synchronous generators (PMSG). Each of these generator types has its own unique characteristics and benefits, making them suitable for different applications depending on factors such as power output requirements, environmental conditions and cost considerations. While all three generator types can be utilized in medium and large-scale WECS. The PMSGs, in particular, due to its relatively simple structure, high power density, gear-less transmission capability, less maintenance, reliability, and ease of control, are considered to be cost-effective solution for small-scale WECS [5–8].

Four main MPPT control strategies are commonly discussed in the literature on WECS: optimal torque control (OTC), tip-speed ratio (TSR) control, power signal feedback (PSF) and hill-climbing search (HCS), which is also referred to as the perturbation and observation (P&O) control method. These four methods are widely studied and utilized in research, as reported by various studies [1, 5]. In order to maximize the power generated by a WT, an optimal TSR can be calculated for each individual turbine. The WT rotor speed can then be controlled using the TSR control approach to maintain this optimal TSR. However, the implementation of a TSR control technique can present two significant challenges. The first step in accurately measuring the wind speed in a system is to use an anemometer, which can increase the overall cost of the system. Secondly, since the optimal TSR value varies among different systems, it must be determined for each specific system, as highlighted by various studies [5, 9, 10].

In general, the OTC is not only easy to use but also quick and effective. The inability to directly measure wind speed, however, causes its efficiency to be lower than that of the TSR technique [1]. The difference between TSR and OTC approaches is minimal, according to [2]. On the other hand, prior knowledge of the WT maximum power curve is required for PSF control, which is typically obtained through either simulations or experimental tests. This dependency on the maximum power curve presents a challenge for implementing a PSF technique, as it can be costly and complex, as noted in various studies [10]. The HCS control technique, unlike the TSR approach, does not require prior knowledge of the maximum power curve. However, under rapid wind speed variations, HCS may not achieve MPPT, and determining an appropriate step-size can also be challenging. A larger step-size results in faster convergence but also increased oscillations around the MPP, causing a compromised efficiency. Conversely, a smaller step-size improved efficiency but led to slower convergence [1].

The use of hybrid control approaches and artificial intelligence (AI)-based methodologies, has eradicated majority of the aforementioned demerits/challenges. Insensitivity and faster convergence to parameter fluctuation, and acceptance of noisy and imperfect signals are only a few benefits of the fuzzy logic control (FLC) [11]. By employing an inverse-turbine model, neural network (NN)-based schemes can also be employed to alleviate the issues related to speed of wind measurement or estimate. This model can be used as a virtual anemometer by es-

timating the wind speed from the actual torque and speed [12].

The hybrid control approaches, combining the benefits of multiple techniques, have been widely researched in order cope with multiple limitations at a time. For instance, [2] combined the OTC with HCS to address the problems associated with conventional HCS under rapid wind speed variation, and to avoid the speed-efficiency trade-off. Another study combined a PSF control with HCS to develop a flexible, sensor-less technique that can be applied to different types of WTs [1].

The MPPT algorithms utilize control algorithms with a primary requirement of robustness. Sliding mode control (SMC) is one such algorithm, characterized as a generalized and robust nonlinear technique [13]. The inherent invariance in sliding phase makes them even more appealing when performance and robustness are concerned [14]. The inherent discontinuous nature of the controller however caused high-frequency oscillations about the switching manifold, phenomenon known as chattering, which is coped with the higher-order variants, super-twisting algorithm (STA) and real-twisting algorithm (RTA), of the SMC [15]. The SMC has been widely utilized as MPPT algorithms in recent literature citea18,zaheer,mppt1

This study proposes ANN based SMC variants, observer-based SMC, IBSMC, and reaching law-based STA, to attain MPPT in PMSG-WECS. These designs offer fast and accurate asymptotic convergence to the equilibrium with notable robustness against uncertainties and ambient variations. Furthermore, the simple structure of STA and its promulgated nature of diminishing chattering are portraying it superior in terms of dynamic performance.

The manuscript is structured in the following order. Table 1 summarizes all the critical abbreviations used in the manuscript. A brief introduction to WECS is established in Section 2 followed by a detailed process of transforming the system from input-output form in Section 3. Derivative of the shaft velocity,

Table 1
List of abbreviations

Entity	Description
ANN	Artificial function-fitting neural network
FOSMC	First order SMC
HGO	High gain observer
HSS	High shaft speed
IBSMC	Integral back-stepping SMC
MPP	Maximum power point
MPPT	Maximum power point tracking
MSE	Mean squared error
PMSG	Permanent magnet synchronous generator
RTA	Real-twisting algorithm
SMC	Sliding mode control
STA	Super-twisting algorithm
TSR	Tip-speed ratio
VSWT	Variable speed wind turbine
WECS	Wind energy conversion system
WT	Wind turbine

using a HGO, is outlined in Section 4 and Section 5 discusses the estimation of nonlinear drifts using ANN. Controllers design is covered in Section 6. A discussion on the robustness and performance of the proposed algorithms, based on simulation results, is presented in Section 7 while the concluding remarks are included in Section 8.

2. SYSTEM DESCRIPTION

A wind energy conversion system (WECS) is characterized as a technology that take kinetic energy from wind and transforms it into precious electrical energy for domestic as well as commercial purposes. WECS, as depicted in Fig. 1, consists of a wind turbine (WTs), which is a large device with blades that rotate when wind blows on them. The WTs are coupled, mechanically via a shaft and gearbox, with a generator (PMSG in this case) which takes the wind kinetic energy, accumulated by WTs, as input to generate electricity.

2.1. Wind turbine (WT) modeling

Mathematical model of a WT, portraying its behavior and performance under various operating conditions, is an important aspect of the design process. It is used to predict the power output, aerodynamic loads, and response to environmental conditions, thereby enabling engineers to optimize its design and control strategies. Moreover, simulation of mechanical behavior of a turbine components (shaft and gearbox) is an other pro-

nounced aspect of WT modeling. This is necessary to ensure that the turbine can withstand the mechanical stresses induced by the wind and operate reliably over its lifespan. Regulation of turbine speed and power output is synthesized with ease using WT models. A typical WT behavior to various wind speeds is depicted in Fig. 2.

The power at the WT shaft, generated by aerodynamics (kinetic energy carried by wind), depending upon various WT parameters, is expressed mathematically as follows [18]:

$$P_{mec} = \frac{1}{2} \rho \pi R_{tb}^2 v_{wd}^3 C_{pr}(\lambda, B), \quad (1)$$

where, R_{tb} is the radius of the WT blade, ρ is the density of incoming air with speed v_{wd} and C_{pr} is the coefficient of power, which is a nonlinear function of pitch angle (B , which is considered to have constant values at different wind speeds) and TSR and is an indication of WT efficiency. An optimum value of TSR (λ_{opt}) results in maximum value of C_{pr} represented as $C_{pr_{mx}}$. In general, extraction of maximum power (up to nominal speed) and attainment of λ_{opt} is subjected to shaft-speed adjustment by a VSWT. Typical values of the transmission ratio (i_{tr}) and turbine high speed shaft (HSS) angular speed (Ω_{hss}) are listed in Table 2.

The information for $C_{pr}(\lambda)$ can be mathematically described by considering ($\lambda = B$) as follows:

$$C_{pr}(\lambda) = \lambda(0.0061 - 0.0013\lambda + 0.0081\lambda^2 - 0.0009\lambda^3) \quad (2)$$

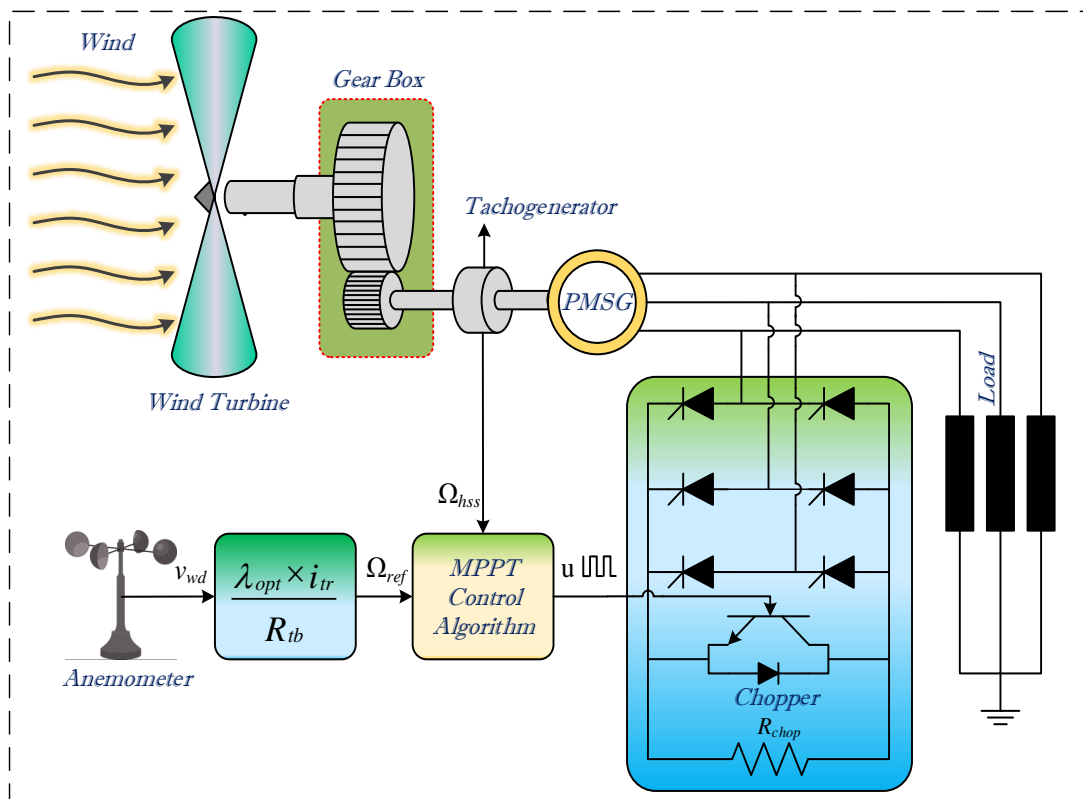


Fig. 1. Variable speed PMSG-WECS

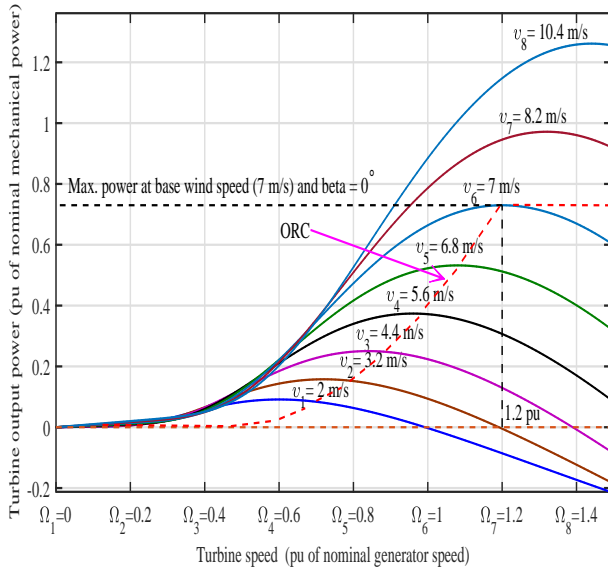


Fig. 2. The relationship between turbine power and turbine speed at various wind speeds

Table 2
Wind turbine and PMSG parameters

Name	Quantity	Value
Wind turbine	Density of air mass, ρ	1.250 kg/m ³
	Radius of turbine blade, R_{tb}	2.50 m
	TSR, λ_{opt}	7.0
	Transmission or gear ratio, i_{tr}	7.0
	Power coefficient, C_{pmax}	0.4760
	Wind speed average value, v_{wd}	7.0
PMSG	Generator stator resistance, R_{se}	3.3 Ω
	Load inductance, L_{ch}	0.008 H
	PM flux constant, ϕ_{con}	438.2 mWb
	Pole pairs number, p_p	3.0
	Stator $d = q$ -axis inductance, $L_d = L_q$	41.560 mH
	Shaft inertia, J_{hs}	0.0552 kg m ²

while the TSR has the following mathematical representation:

$$\lambda = \frac{\Omega_{hss} R_{tb}}{v_{wd} i_{tr}}. \quad (3)$$

The transmission ratio, represented as i_{tr} and Ω_{hss} (in rad/s) are used to describe the available aerodynamic mechanical power at the WT shaft, as per the relation given in [18]. Table 2 provides typical values for these parameters.

Power (P_{mec}) at the blades causes an introduction of torque at the turbine shaft, denoted as Γ_{mec} . The Γ_{mec} , as a function of the torque coefficient ($C_\tau(\lambda)$) has the following mathematical representation:

$$\Gamma_{mec} = \frac{1}{2} \rho \pi R_{tb}^3 v_{wd}^2 C_\tau(\lambda), \quad (4)$$

where

$$C_\tau(\lambda) = \frac{C_{pr}(\lambda)}{\lambda}. \quad (5)$$

Having outlined all relevant information, it is now appropriate to present mathematically the model for PMSG.

2.2. PMSG modeling

The mathematical model for PMSG is given in the dq -axes form is adopted from [18]. The equations are as follows:

$$\begin{aligned} \dot{i}_d &= \frac{-R_{se} i_d + p_p (L_q - L_{chop}) \Omega_{hss} i_q - R_{chop} i_d}{(L_d + L_{chop})}, \\ \dot{i}_q &= \frac{-R_{se} i_q - p_p (L_q + L_{chop}) \Omega_{hss} i_d - R_{chop} i_q}{(L_q + L_{chop})} \\ &\quad + p_p \Omega_{hss} \phi_{con}, \\ \dot{\Omega}_{hss} &= \frac{1}{(J_{hs})} \left[-p_p \phi_{con} i_q + \frac{d_1 v_{wd}^2}{i_{tr}} + \frac{d_2 v_{wd} \Omega_{hss}}{i_{tr}^2} \right. \\ &\quad \left. + \frac{d_3 \Omega_{hss}^2}{i_{tr}^3} \right]. \end{aligned} \quad (6)$$

In these equations: dot ($\dot{\cdot}$) represents the time derivative, i.e., $\frac{d}{dt}$. The stator resistance, inductance and current along d -axis and inductance and current along q -axis are represented by R_{se} , L_d , i_d , L_q and i_q respectively. Usually, $L_d = L_q$ for a non-salient pole PMSG. The high speed shaft (HSS) angular speed and inertia are represented by Ω_{hss} and J_{hs} respectively. Constant flux due to a permanent magnet (PM) is denoted with Φ_{con} while transmission ratio and number of pole pairs are represented with i_{tr} and p_p respectively. Finally, R_{chop} and L_{chop} represent the chopper equivalent resistance and inductance respectively.

A common rule of thumb is utilized to simplify the notation with a simplified/generalized nomenclature for the state variables resulting in $[i_d \ i_q \ \Omega_{hss}]^T = [x_1 \ x_2 \ x_3]^T$. A compact representation of the system, using the parameters mentioned, can be expressed through its simplified state-space equation as:

$$\begin{bmatrix} \dot{x}_1 \\ \dot{x}_2 \\ \dot{x}_3 \end{bmatrix} = \begin{bmatrix} -(\ell_1 + \ell_3 R_{chop}) - (\ell_2 x_3) + 0 \\ -(\ell_5 x_3) - (\ell_4 + \ell_7 R_{chop}) + \ell_6 \\ -\frac{\ell_8 v_{wd}^2}{x_1} - \frac{\ell_{11}}{J_{hs}} - (\ell_9 v_{wd} + \ell_{10} x_3) \end{bmatrix}^T \begin{bmatrix} x_1 \\ x_2 \\ x_3 \end{bmatrix}, \quad (7)$$

where ℓ_1 to ℓ_{11} are constants, specified in Table 3 and are outlined here as: $\ell_1 = \ell_4 = R_{se}/(L_d + L_{chop})$, $\ell_2 = p_p(L_q - L_{chop})/(L_d + L_{chop})$, $\ell_3 = \ell_6 = 1/(L_d + L_{chop})$, $\ell_5 = p_p$, $\ell_6 = \ell_{11} = p_p \phi_{con}$, $\ell_8 = -d_1/(i_{tr} J_{hs})$, $\ell_9 = -d_2/(i_{tr}^2 J_{hs})$, and $\ell_{10} = -d_3/(i_{tr}^3 J_{hs})$.

Table 3

Constant terms of PMSG-WECS

Entity	Value	Entity	Value	Entity	Value
ℓ_1	27.147	ℓ_4	27.147	ℓ_8	9.945
ℓ_2	0.94866	ℓ_5	3	ℓ_9	0.1332
ℓ_3	8.2264	ℓ_6	1.3146	ℓ_{10}	0.00506
0	0	ℓ_7	8.2264	ℓ_{11}	23.806

3. THE INPUT-OUTPUT COORDINATES TRANSFORMATION

WECS representative model, equation (7), has the following standard representation.

$$\dot{x}(t) = \mathcal{F}(x(t)) + \mathcal{G}(x(t))u(t) + \Delta(x(t), t), \quad (8)$$

$$y(t) = h(x(t)) = x_3, \quad (9)$$

where $x(t): \mathfrak{R} \times \mathfrak{R}^n \rightarrow \mathfrak{R}^n$ defines the state vector, $u(t) \in \mathfrak{R}$, represents the control input, $\Delta(x(t), t): \mathfrak{R} \times \mathfrak{R}^n \rightarrow \mathfrak{R}^n$, is the matched uncertainty, and the two smooth vector fields $\mathcal{F}(x(t))$ and $\mathcal{G}(x(t))$, which are non-linear in nature, can be mathematically represented as follows:

$$\begin{aligned} \mathcal{F}(x) &= \begin{bmatrix} f_1 \\ f_2 \\ f_3 \end{bmatrix} = \begin{bmatrix} -\ell_1 x_1 - \ell_2 x_2 x_3 \\ -\ell_4 x_2 - \ell_5 x_1 x_3 + \ell_6 x_3 \\ -\ell_8 v_{wd}^2 - \ell_9 v_{wd} x_3 - \ell_{10} x_3^2 - \ell_{11} x_2 \end{bmatrix}^T, \\ \mathcal{B}(x) &= \begin{bmatrix} -\ell_3 x_1 \\ -\ell_7 x_2 \\ 0 \end{bmatrix}, \\ u(t) &= R_{chop}. \end{aligned} \quad (10)$$

The primary goal is to control the output, i.e., $y(t) = x_3 = \Omega_{hss}$. So, the subsequent equations (7) can easily convert into input-output form [18] as follows:

$$\begin{aligned} z_1 &= y = \Omega_{hss} = x_3, \\ z_2 &= L_f h(x) = \frac{\partial h(x)}{\partial x} f(x) = -n_1 - n_2 x_3 - n_3 x_3^2 - n_4 x_2, \quad (11) \\ z_3 &= L_f^2 h(x) = \frac{x_1}{x_2}, \end{aligned}$$

where

$$n_1 = \ell_8 v_{wd}^2, \quad n_2 = \ell_9 v_{wd}, \quad n_3 = \ell_{10} \quad \text{and} \quad n_4 = \ell_{11}.$$

It may be noted that relative degree (r) of the system is less than system order ($n = 3$) causing output to depend upon the input and its derivatives. As a result, the input-output form can be expressed as in equation (12).

$$\begin{aligned} \dot{z}_1 &= z_2, \\ \dot{z}_2 &= \underbrace{-n_4 f_2(x) - (n_2 + 2n_3 x_3) f_3(x)}_{L_f^2 h(x)} + \underbrace{\ell_3 x_1 n_4 x_2 u}_{L_g L_f h(x)}, \\ \dot{z}_3 &= -\ell_1 z_3 - \ell_2 z_1 - \ell_3 x_1 z_3 u \\ &\quad - z_3 \left(-\ell_1 - \ell_5 z_1 z_3 + \frac{\ell_{11} z_1 n_4}{n_1} - \ell_3 x_1 u \right), \end{aligned} \quad (12)$$

where z_3 is the zero dynamic state. Hence, it can be disregarded on the condition that it remains stable. If this state variable is stable, meaning that its behavior over time is predictable and does not result in instability, it can be safely ignored in the control system design. In other words, the control system can be simplified by neglecting this state variable and its associated

dynamics, without significantly impacting the overall behavior of the system.

3.1. Zero dynamic stability

During the conversion of input-output for a nonlinear system, its dynamics can be divided into two components - an internal part (state z_3) and an external part (states z_1 and z_2). The external part can be directly controlled by manipulating the input u , while the stability of the internal part can be easily determined by locating the system zeros, as discussed in [19].

The zero dynamics, obtained by letting $z_1 = z_2 = u = 0$ in equation (12) resulting in:

$$\dot{z}_3 = -z_3(\gamma_1 - \alpha_1). \quad (13)$$

The internal dynamics remain stable as long as γ_1 is greater than α_1 .

4. HIGH GAIN OBSERVER MODELING

Dependence of the controllers/algorithms on the derivatives of the output and/or switching surface, due to the deficient relative degree as coined in the previous section, demands an efficient technique in practical realizations. The technique is required to estimate the derivatives without amplifying system noise. One such technique is the high gain observer (HGO), exhibiting rapid convergence towards the initial values. Therefore, it has been assumed that the output z_1 (i.e., $z_1 = x_3$) is twice differentiable with bounded (by constant $L > 0$) second derivative. Let ζ_1 represent a mismatch between the z_1 and its estimate \hat{z}_1 in the absence of noise as follows:

$$\zeta_1 = (z_1 - \hat{z}_1). \quad (14)$$

The first-order system, also known as the HGO (see equations (15)), can be used to compute the estimated output \hat{z}_1 and its derivative \hat{z}_2 shown in Fig. 3.

$$\dot{\hat{z}}_1 = \hat{z}_2 + \frac{\alpha_1}{\psi_2}(\zeta_1), \quad (15)$$

$$\dot{\hat{z}}_2 = D_n z_1 + \frac{\alpha_2}{\psi_2^2}(\zeta_1), \quad (16)$$

where α_1 , α_2 and ψ_2 are positive gains given in Table 5. Equation (15) can also be written as [20]:

$$\dot{x} = Q_n x + \alpha(\psi) \times (\zeta_1) + D_n z_1, \quad (17)$$

where $a(\psi) = \left[\frac{\alpha_1}{\psi_2}, \frac{\alpha_2}{\psi_2^2}, \dots, \frac{\alpha_n}{\psi_2^n} \right]$ and $0 < \zeta_1 < \bar{\zeta}_1$. Besides,

$$D_n = \begin{bmatrix} 0_{(n-1) \times 1} & I_{(n-1) \times (n-1)} \\ 0_{1 \times 1} & 0_{1 \times (n-1)} \end{bmatrix} \quad \text{and} \quad Q_n = \begin{bmatrix} 0_{(n-1) \times 1} \\ I_{1 \times 1} \end{bmatrix}.$$

The overall closed loop stability of the closed loop system, with HGO in the loop, is subjected to fast convergence of HGO while maintaining boundedness [20].

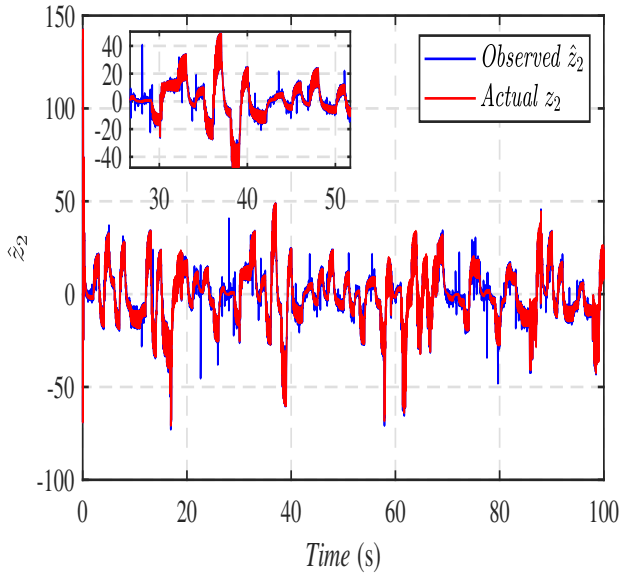


Fig. 3. HGO Actual and observed states

5. LEVENBERG-MARQUARDT ALGORITHM BASED FUNCTION FITTING NEURAL NETWORK FOR NONLINEAR FUNCTIONS ESTIMATION

This section describes the strategy for estimation of Lie-derivatives via function-fitting neural-network (FN), a multiple-input-single-output (MISO) system, with Levenberg-Marquardt algorithm. The Levenberg-Marquardt algorithm adjusts the biases and weights of the NN for minimizing a difference between the predicted outputs and an actual target output/s (mean-squared-error (MSE)), given a set of inputs.

Let us denote the input data set as $\mathbf{X} = [z_1, z_2, z_3, v_{wd}] \in \mathfrak{R}^{n \times d}$, where n and d represent number of data points and dimensionality of input respectively. Moreover, $\mathbf{Y} = L_g L_f h(x) \in \mathfrak{R}^{n \times m}$ is representative of target output/s with m representing the output dimensionality.

A neural network can be represented as a function $f_{\theta} : \mathfrak{R}^d \rightarrow \mathfrak{R}^m$, where θ denotes the set of weights and biases of the network. The function $f_{\theta}(x)$ takes an input $x \in \mathfrak{R}^d$ and produces an output $y \in \mathfrak{R}^m$.

The Levenberg-Marquardt algorithm minimizes the following objective function,

$$\min_{\theta} \frac{1}{2} \sum_{i=1}^n \|f_{\theta}(x_i) - y_i\|^2 + \frac{\lambda_a}{2} \sum_{j=1}^p \theta_j^2, \quad (18)$$

where $\|\cdot\|$ denotes the Euclidean norm, λ_a is a regularization parameter that controls a trade-off between fitting the data and controlling over-fitting, and p represents number of weights and biases in the network. The first term in the objective function (equation (18)) measures the MSE while the second term adds a penalty for large values of the weights and biases. The Levenberg-Marquardt algorithm iteratively updates the weights and biases of the network to minimize this objective function.

A trained FN is ready to generate/estimate an output for any arbitrary input. The estimated Lie-derivatives are compared

with the actual ones as shown in Fig. 4 and Fig. 5 while parameters are listed in Table 4.

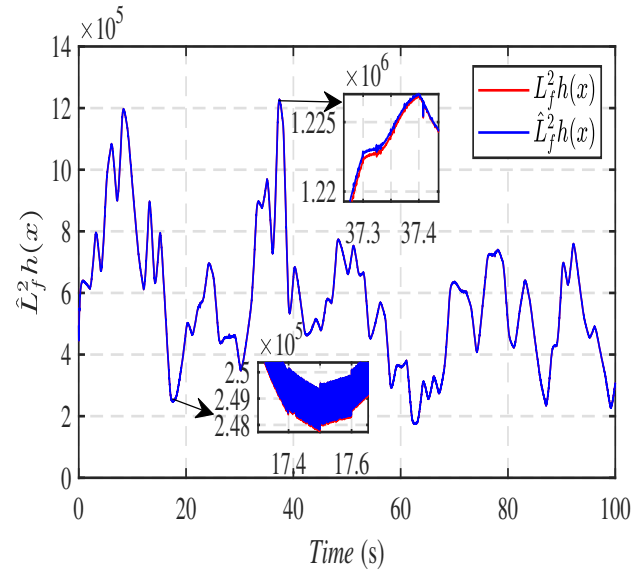
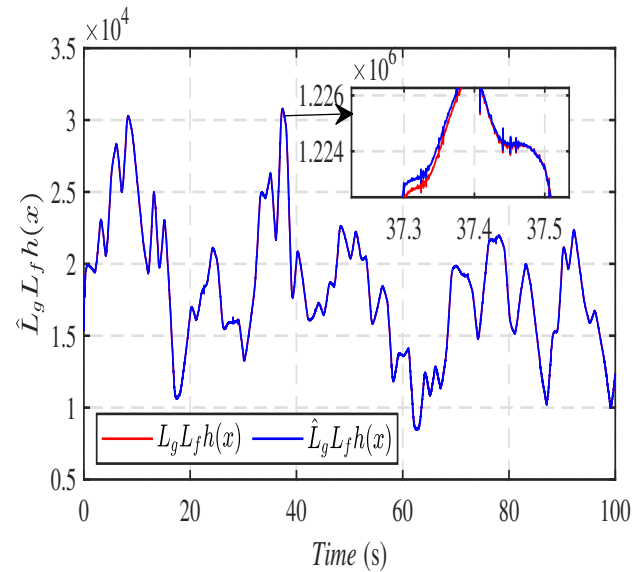
Fig. 4. Actual and estimated $L_f^2 h(x)$ Fig. 5. Actual and estimated $L_g L_f h(x)$

Table 4

Various training parameters for ANN based FN

S. No.	Parameters	Description
1	Number of inputs to ANN	4
2	Number of outputs of ANN	1
3	Training algorithm	Levenberg-Marquardt
4	No. of hidden layers	2
5	No. of hidden neurons	2
6	No. of validation checks	0-6
7	No. of iterations	100

6. PROPOSED CONTROL SCHEME FOR MPPT

The previous sections have covered the conversion of the system into its normal form and the estimation of the output derivative. The grounds are now set to devise an MPPT to extract maximum power out of the system by operating the PMSG-WECS at its MPP (see Fig. 6). In contrast to this, SMC, IBSMC and STA based SMC have been designed and will be discussed in the next section.

6.1. Sliding mode control (SMC) design

SMC is an effective nonlinear technique used in a variety of control applications. The primary goal of SMC is to force a sliding manifold, a linear combination of states, to zero and hence system states to an equilibrium along that manifold. Initially, the system states are directed to the switching manifold by a discontinuous control law (the phase known as reaching phase) and then are confined there by the same controller. Moreover, the Hurwitz nature of the switching manifold causes the confined trajectories to move towards stable equilibrium (the phase known as sliding phase). The primary advantage comes in *sliding phase*, where the system dynamics are of reduced order and are invariant to disturbances and system parametric variations, making it suitable for controlling nonlinear and uncertain systems.

Overall, the design of chattering-free SMC involves defining a switching surface, developing a control law that enforces sliding mode motion, and ensuring that the system trajectory slides along the sliding manifold without chattering. In a nutshell, re-

duction in system order and robustness to disturbances are some of the key advantages of SMC.

In tracking applications, an error based sliding manifold is usually preferred followed by a control law which is a combination of an equilibrium/equivalent control input $u_{eq}(t)$ and a disturbance/discontinuous control input $u_{dis}(t)$. These, altogether accomplish the reaching and sliding phase, guaranteeing reference tracking.

Now, the error/mismatch can be defined as:

$$e(t) = z_1 - \Omega_{1ref}(t). \quad (19)$$

In order to simplify the notation, the variable $\Omega_{ref}(t)$ will be denoted as z_{1ref} in all future discussions. This change in notation will make it easier to refer to the reference value of the system angular velocity.

The time derivative of equation (19) is computed as in equation (20).

$$\dot{e}(t) = \frac{d}{dt}(z_1 - z_{1ref}) = \dot{z}_1 - \frac{d}{dt}(z_{1ref}) = \dot{z}_1 - \dot{z}_{1ref}. \quad (20)$$

In the actual implementation, only the system angular velocity z_1 is directly measured, and its derivative is estimated using the HGO technique discussed in the previous section. Therefore, in the context of equation (20), we can replace \dot{z}_1 with the estimated derivative of z_1 , denoted as \hat{z}_2 :

$$\begin{aligned} \dot{e}(t) &= \hat{z}_2 - \dot{z}_{1ref} \\ \ddot{e}(t) &= \frac{d}{dt}(\hat{z}_2 - \dot{z}_{1ref}) = \frac{d}{dt}\hat{z}_2 - \frac{d}{dt}(\dot{z}_{1ref}). \end{aligned} \quad (21)$$

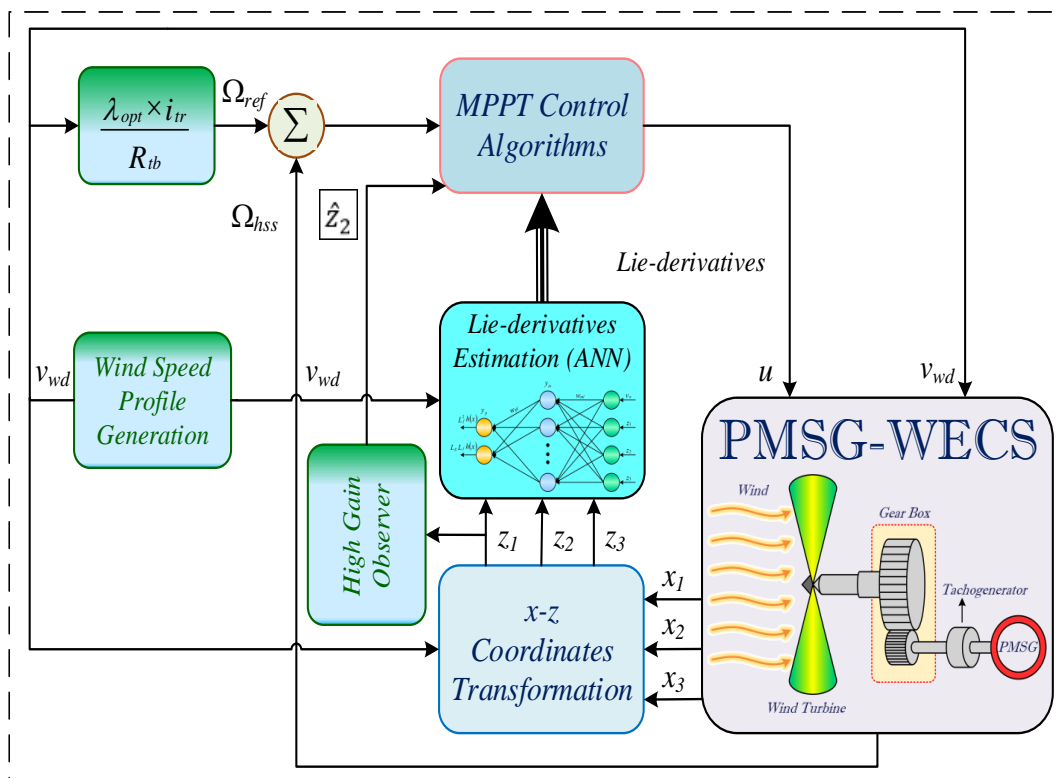


Fig. 6. ANN and HGO based closed loop PMSG-WECS

Using the dynamics of the system in equation (12), we can substitute for $\frac{d}{dt}\hat{z}_2$ and $\frac{d}{dt}(\dot{z}_{1\text{ref}})$ as follows:

$$\begin{aligned}\ddot{e}(t) &= \hat{L}_f \hat{L}_g h(x) - \hat{L}_f^2 h(x) - \hat{L}_g L_f h(x) u \\ &= \hat{L}_f^2 h(x) + \hat{L}_g L_f h(x) u.\end{aligned}\quad (22)$$

The SMC design starts with definition of Hurwitz sliding manifold over the state space of the system.

Remark 1. Hurwitz nature of the surface guarantee that the trajectories *slide* towards stable equilibrium.

An integral-derivative type surface is defined in equation (23) below where the integral term is providing a low pass filtering effect and hence smoothness.

$$s(x) = \mu_1 e(t) + \dot{e}(t) + \mu_2 \int_0^t e(t) dt. \quad (23)$$

The positive constants, μ_1 and μ_2 outlined in Table 5, are the performance defining terms of the sliding mode (reduced order) dynamics.

A controller is desired to force the trajectories to $s(x)$, and once reached, confine them thereafter. A result is the attainment of $s(x) = 0$ and hence $e(t) \rightarrow 0$.

Taking the time derivative of equation (23) with respect to equation (12).

$$\dot{s}(x) = (\dot{\hat{z}}_2 - \dot{z}_{1\text{ref}}) + \alpha_1 (\hat{z}_2 - z_{1\text{ref}}) + \alpha_2 e(t). \quad (24)$$

This approach involves considering a strong reachability condition (u_{dis}) and employ an equivalent controller of the form,

$$u = u_{\text{eqv}} - \left(\underbrace{\mu_3 s + \mu_4 \text{sign}(s)}_{u_{dis}} \right), \quad (25)$$

where

$$\begin{aligned}u_{\text{eqv}} &= \frac{1}{\hat{L}_g L_f h(x)} [\dot{z}_{1\text{ref}} - \mu_1 \hat{z}_2 - \mu_2 z_1 + \mu_1 \dot{z}_{1\text{ref}} + \dots \\ &\quad + \mu_2 z_{1\text{ref}} - \hat{L}_f^2 h(x)].\end{aligned}$$

The choice of u in equation (25), with μ_3 and μ_4 being the positive gains which can be tuned for a desired response and are outlined in Table 5, gives the following surface dynamics.

$$\dot{s} = -\mu_3 s - \mu_4 \text{sign}(s). \quad (26)$$

Use of a positive definite and radially unbounded function $\mathcal{V}(t) = \frac{1}{2}s^2$ in combination to equations (23), (25) and (26) dictate an asymptotic stability of the overall closed loop system.

$$\begin{aligned}\dot{\mathcal{V}}(t) &= s\dot{s} \\ &= -\mu_3 s^2 - \mu_4 |s| \leq 0.\end{aligned}\quad (27)$$

The negative definiteness of the derivative of energy like function $\mathcal{V}(t)$, in equation (27), reveals the fact that sliding modes are enforced.

It is worth noting that this is the traditional control law that exhibits chattering. The upcoming algorithms based HOSM (BISMIC and STA) are designed to suppress the *chattering*.

6.2. IBSMC based MPPT control strategy design

In this section, an MPPT strategy based on IBSMC is presented. The goal of this strategy is to address the limitations of the standard SMC, which were discussed in Section 6.1. The IBSMC-based MPPT technique is designed with the aim of enhancing the WECS capacity to track the MPP, thereby enhancing its overall performance. By using this strategy, the WECS can operate at its optimal efficiency while also overcoming the negative impacts of varying wind speeds and other environmental factors. The proposed approach is expected to lead to more effective power generation, which can be particularly beneficial for remote or off-grid applications.

The subsequent steps delineate the process of designing the IBSMC algorithm [21].

Step 1: Use the tracking error and its derivative of equations (19) and (20) with the following notations:

$$\begin{aligned}e_1 &= e, \\ e_2 &= \dot{e}.\end{aligned}$$

Step 2: The suggested control law (IBSMC) can be defined as follows using the standard ISMC [21]:

$$u = u_i + u_d, \quad (28)$$

where the continuous control component u_i can be created through linear state feedback (see equation (29)) while the discontinuous control component u_d can be established through the utilization of a back-stepping design approach.

$$u_i = -\sigma_1(e_1) - \sigma_2(e_2), \quad (29)$$

where σ_1 and σ_2 represent the gains.

Step 3: Design u_d using the back-stepping approach, which requires selecting a Lyapunov function candidate $V_1(e_1)$ that satisfies three conditions: positive definiteness, radial unboundedness, and negative definiteness of its time derivative. A suitable $V_1(e_1)$ is defined as:

$$V_1(e_1) = \frac{1}{2}e_1^2. \quad (30)$$

Differentiating V_1 with respect to time and simplifying equations (19) and (20) using the system equations yields:

$$\dot{V}_1 = e_1 \dot{e}_1 = e_1 (\dot{z}_1 - \dot{z}_{1\text{ref}}) = e_1 (\hat{z}_2 - \dot{z}_{1\text{ref}}). \quad (31)$$

If one view z_2 in equation (31) as a virtual controller that serves to stabilize the system, it can be represented in the following way:

$$z_2^* = -k_2 e_1 + \dot{z}_{1\text{ref}}$$

Robust estimation based nonlinear HOSMC strategies for PMSG-WECS

yields, $\dot{V}_1 = -k_2 e_1^2 < 0$, which exhibits global asymptotic stability.

Step 4: Define an integral switching manifold with z_i as integral term [21, 22].

$$s_1 = z_2 + k_2 e_1 - \dot{z}_{1\text{ref}} + z_i \quad (32)$$

A derivative of equation (32) and its simplification using the system equations given in equations (12) and (28) yields:

$$\dot{s}_1 = \widehat{L}_f^2 h(x) + \widehat{L}_g L_f h(x)(u_i + u_d) + k_2 \dot{e}_1. \quad (33)$$

Now, choosing,

$$\dot{z}_i = -\widehat{L}_g L_f h(x) u_i + \dot{z}_{1\text{ref}} \quad (34)$$

and by putting equation (34) in equation (32) along equation (33), one gets

$$\dot{s}_1 = \widehat{L}_f^2 h(x) + \widehat{L}_g L_f h(x) u_d + k_2 \dot{e}_1. \quad (35)$$

Step 5: A candidate for a composite Lyapunov function, denoted by $V_2(e_1, s_1)$, is defined by the following equation:

$$V_2(e_1, s_1) = \frac{1}{2} (e_1^2 + s_1^2). \quad (36)$$

Differentiating equation (36) and simplifying equation (31) one gets

$$\dot{V}_2 = (e_1 \dot{e}_1 + s_1 \dot{s}_1) = \dot{V}_1 + s_1 \dot{s}_1. \quad (37)$$

Here considering a strong reachability law of the following form as in [23].

$$\dot{s}_1 = (-k_p s_1 - k_q \text{sign}(s_1)). \quad (38)$$

When equation (38) is substituted for equation (37), it results in

$$\dot{V}_2 = \dot{V}_1 + s_1 (-k_p s_1 - k_q \text{sign}(s_1)). \quad (39)$$

Negative definiteness of \dot{V}_2 is desired to ensure asymptotic stability of the overall closed loop system.

Comparing equation (35) and equation (38), one gets

$$u_d = \frac{-1}{\widehat{L}_g L_f h(x)} \left[\widehat{L}_f^2 h(x) + k_2 \dot{e}_1 + k_p s_1 + k_q \text{sign}(s_1) \right]. \quad (40)$$

The final step is to replace u_i and u_d from equations (29) and (40), respectively, in equation (28), to produce the overall proposed IBSMC law as shown below.

$$u_{IBSMC} = \underbrace{\frac{-1}{\widehat{L}_g L_f h(x)} \left[\widehat{L}_f^2 h(x) + k_2 \dot{e}_1 + k_p s_1 + k_q \text{sign}(s_1) \right]}_{u_d} - \underbrace{k_b(e_1) - k_i(e_2)}_{u_i}. \quad (41)$$

Table 5 lists the parameters of the IBSMC law, while its computational flow chart for implementation can be seen in Fig. 7.

Table 5

Overall controllers and HGO Constant parameters

Name	Symbol	Value
SMC	μ_1	103
	μ_2	2000
	μ_3	0.01
	μ_4	50
IBSMC	k_2	0.1
	k_p	100
	k_q	0.001
	k_i	2
	k_b	700
STA	μ_1	103
	μ_2	2000
	ϕ_1	2.3
	ϕ_2	2000
HGO	α_1	3.6
	α_2	9
	ψ_2	0.0004

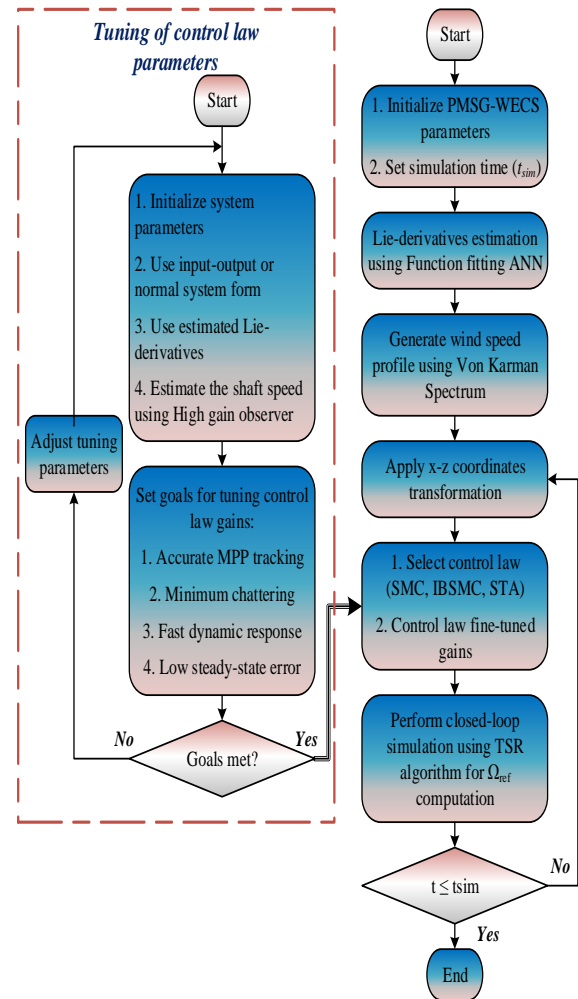


Fig. 7. Computational flow chart of the whole system

6.3. Super-twisting algorithm (STA) design

The STA is a type of SMC that is capable of controlling nonlinear systems even when uncertainties and disturbances are present. The algorithm operates by forcing the system state to follow a desired sliding surface in a finite time, which leads to robust performance in the presence of disturbances and uncertainties. In SMC and IBSMC the switching manifold may exhibit high-frequency vibrations, which can be undesirable in practice. To eliminate this problem, a modified reachability law can be considered instead of the one reported in equation (26).

$$\dot{s} = u_t = -\phi_1 |s|^{0.5} \text{sign}(s) - \phi_2 \int \text{sign}(s) dt, \quad (42)$$

where, ϕ_1 and ϕ_2 are positive scalars given in Table 5. The following sliding mode enforcement law (equation (43)) can be obtained by comparing equation (24) with equation (42).

$$u_{\text{STA}} = \frac{1}{\hat{L}_g L_f h(x)} \left[\underbrace{\ddot{z}_{1\text{ref}} - \mu_1 \dot{z}_2 - \mu_2 z_1 + \mu_1 \dot{z}_{1\text{ref}} + \mu_2 z_{1\text{ref}} - \hat{L}_f^2 h(x)}_{u_{\text{eqv}}} - \underbrace{\phi_1 |s|^{0.5} \text{sign}(s) - \phi_2 \int \text{sign}(s) dt}_{u_t} \right]. \quad (43)$$

In this scenario, u_{eqv} represents the equivalent controller defined in equation (25), while u_t is expressed by equation (42). The attractiveness of the reachability expressed in equation (42) stems from its adaptive gain, which results in a reduction of chattering magnitude as the value of s approaches zero. In addition, the second term undergoes a low-pass filter that removes high-frequency vibrations. As a result, this approach effectively reduces the chattering phenomenon to an acceptable level. Figure 7 depicts the computational flow chart utilized for its implementation.

7. DETAILED SIMULATION RESULTS AND DISCUSSION

To evaluate this work, Fig. 6 depicts the full WECS together with the developed and proposed control schemes, whereas the PMSG-based WECS shown in Fig. 1 has an optimal TSR of $\lambda_{\text{opt}} = 7$ and a maximum power coefficient of $C_{p_{\text{max}}} = 0.476$. The simulations are performed with an average wind speed of 7 m/s. The simulation results are organised in three different cases to assess the potency of the suggested control strategies: 1) variational wind speed profile for, (a) nominal case, (b) varying load varying inertia, 2) deterministic wind speed profile, and 3) comparison of RTA with FL based controller.

In case 1(a), the proposed MPP tracking algorithm is tested under a stochastic wind speed profile. This means that the wind speed varies randomly over time, and the algorithms must be able to track the changes in wind speed in order to maximize the power output of the wind turbine. The simulations are run for a period of 100 seconds, during which the wind speed profile changes randomly. In case 1(b), the robustness of the proposed control schemes is analyzed under a more complex scenario.

The wind speed profile is still stochastic, but in addition, the load and inertia of the wind turbine also vary randomly over time. These variations in load and inertia can have a significant impact on the performance of the control system, and the analysis aims to evaluate how well the proposed control schemes are able to handle these uncertainties. In case 2, the robustness of the proposed control techniques is evaluated in the presence of abrupt variations in the wind speed profile. This means that the wind speed changes suddenly and rapidly, which can pose a challenge for the control system. The goal of this analysis is to determine how well the proposed control techniques can respond to these sudden changes in order to maximize the power output of the wind turbine. In both case 1 and case 2, the proposed controllers (i.e., SMC, IBSMC and STA) are compared with each other.

7.1. Case 1(a): Variational wind speed profile

The initial simulations aim to achieve the maximum power extraction by testing three different control algorithms: SMC, IBSMC and STA. To achieve this objective, the wind turbine is operated at its optimal TSR, denoted by λ_{opt} , which guarantees the best value for the power coefficient $C_{p_{\text{max}}}$. To achieve this, the rotational speed of the PMSG is controlled to ensure that it operates at optimum values. Consequently, all three controllers are capable of tracking the rotational speed of the HSS, while maintaining the TSR at its optimal value and the coefficient of power at its maximum value of $C_{p_{\text{max}}} = 0.476$.

In terms of reference tracking, the comparison in Fig. 8 shows that the control by SMC exhibits oscillatory behavior with a significant steady-state error. In contrast to SMC, the IBSMC algorithm exhibits oscillatory tracking around the reference with reduced amplitude, resulting in lower chattering. On the other hand, the STA control algorithm has a bare minimum steady-state error, superior to both SMC and IBSMC. The convergence time is also much faster for STA, as demonstrated in the zoomed portion of Fig. 8, with STA converging at 0 sec-

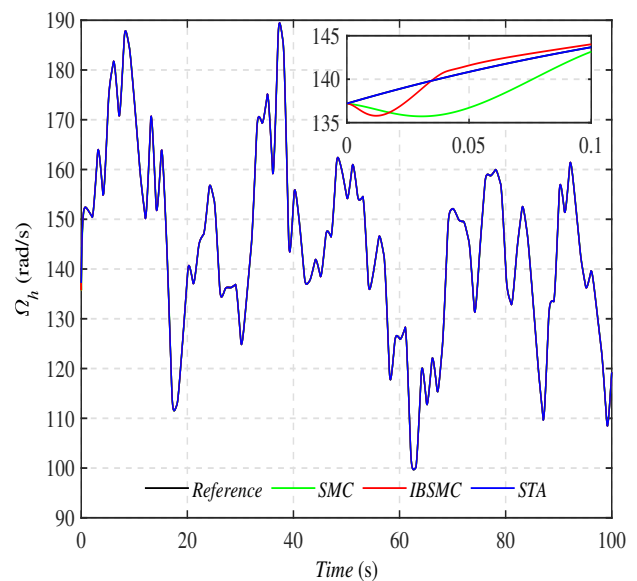


Fig. 8. Desired and actual, HSS angular speeds

Robust estimation based nonlinear HOSMC strategies for PMSG-WECS

onds, IBSMC converging at 0.01 seconds, and SMC converging at 0.1 seconds. Furthermore, the power coefficient C_p and TSR (λ) in Fig. 9 and Fig. 10 achieved by STA are more appealing compared to IBSMC and SMC, making MPPT more effective with STA. Similarly, the mechanical power in Fig. 11 of the shaft around the optimal regime is superior for STA and IBSMC compared to SMC, confirming the elimination of chattering. This can be observed from the zoomed sections of the reference tracking, TSR, C_p , and mechanical powers in the respective figures. Overall, the results show that STA is the best controller for achieving optimal performance in terms of power extraction and chattering reduction.

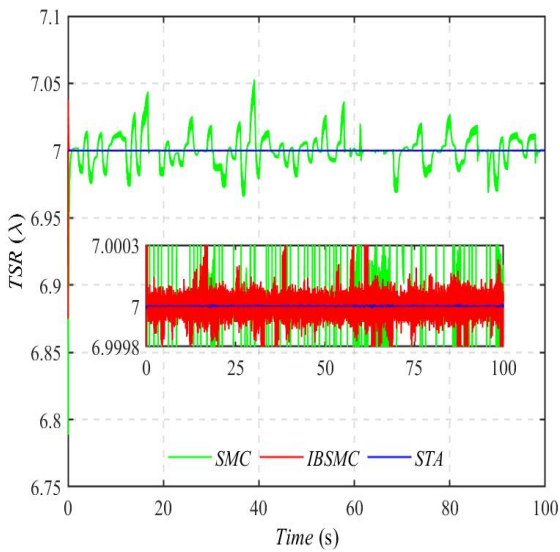


Fig. 9. Tip speed ratio versus time plot

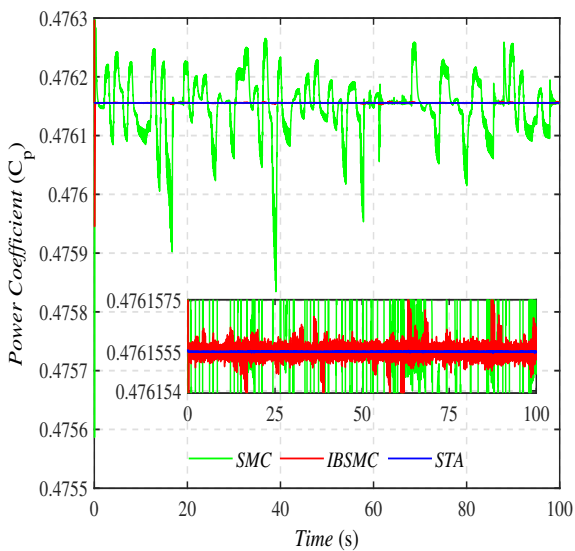


Fig. 10. Coefficient of turbine power versus time

The results of the analysis are presented graphically in Figs. 12, and 13 where electromagnetic torque (Γ_{em}), mechanical power on the generator side ($P_{m_{HSS}}$) are plotted against

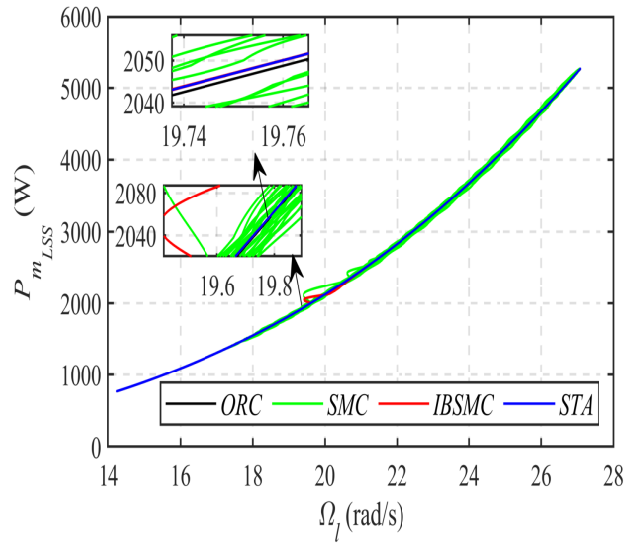


Fig. 11. Turbine shaft speed versus aerodynamic power

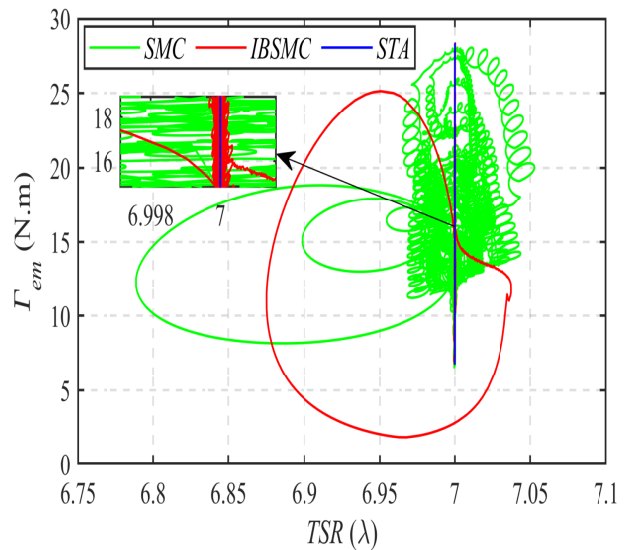


Fig. 12. TSR versus electromagnetic torque

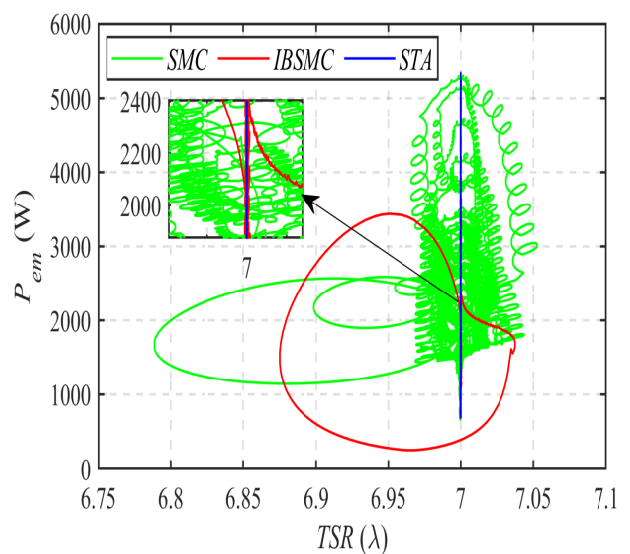


Fig. 13. Mechanical power versus TSR

the TSR (λ) respectively. Figure 14 shows the response of the mechanical torque (Γ_{mec}) to the variations in the turbine shaft speed. The variations of mechanical torque around ORC are smoothly tracked in the case of IBSMC and STA, indicating a reduction in chattering. The results demonstrate that STA outperforms IBSMC, and both outperform the SMC in terms of overall performance. Therefore, it is advisable for power engineers to use model-based STA over the SMC.

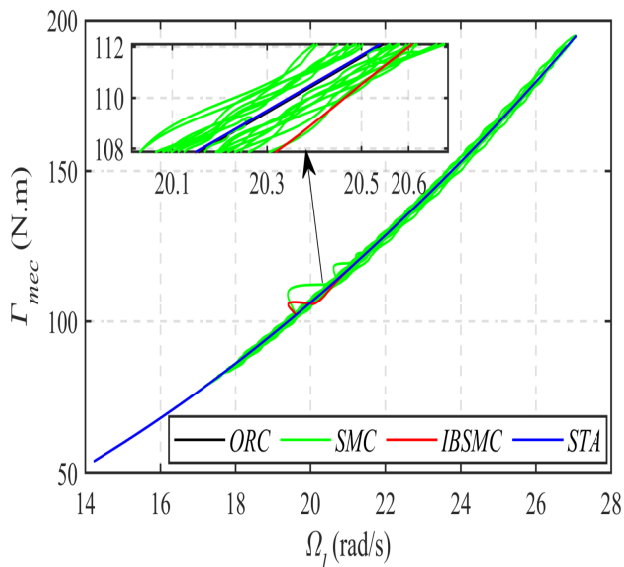


Fig. 14. Turbine shaft speed versus mechanical torque

7.2. Case 1(b): Varying load varying inertia

After analyzing how well the proposed controller techniques track the maximum power point (MPP), their ability to handle challenging conditions is tested. The system’s performance is evaluated under varying loads and inertia. Figure 15 shows the changes in load inductance and inertia over a time period

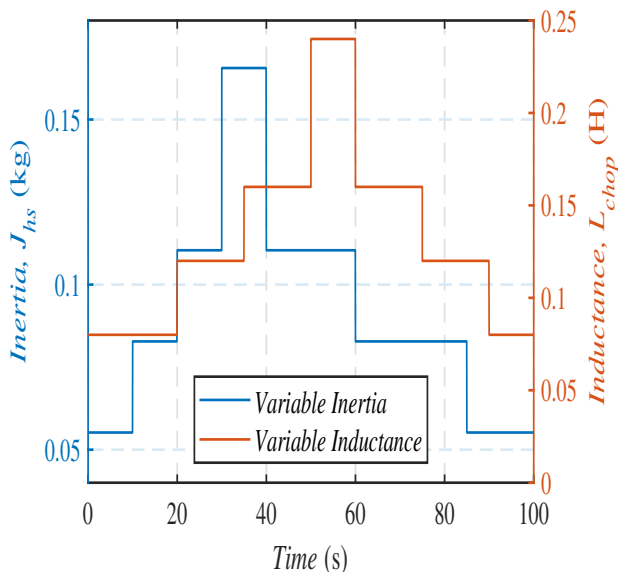


Fig. 15. Varying inertia, varying load inductance profiles

of 0–100 seconds. Model-based STA controller exhibits better HSS side angular speed tracking, as seen in the zoomed section of Fig. 16 at 37.4 seconds, compared to other techniques that experience undershoots during sudden changes in tracking, potentially decreasing power extraction. Although SMC and IBSMC show statistical errors and disturbances in their tip speed ratios and power coefficients, the STA exhibits no such disturbances, as shown in Figs. 17 and 18. SMC C_p drops to a low value of about 40%, but the STA maintains C_p at an optimum value, ensuring robustness against parametric variations and providing MPP. Figures 19 and 20 show variations in TSR with low and high speed shaft powers and with electromagnetic torque, but the STA remains constant at its optimal TSR and C_p , while SMC and IBSMC change their behavior. To maximize wind power capture and reduce chattering, the turbine

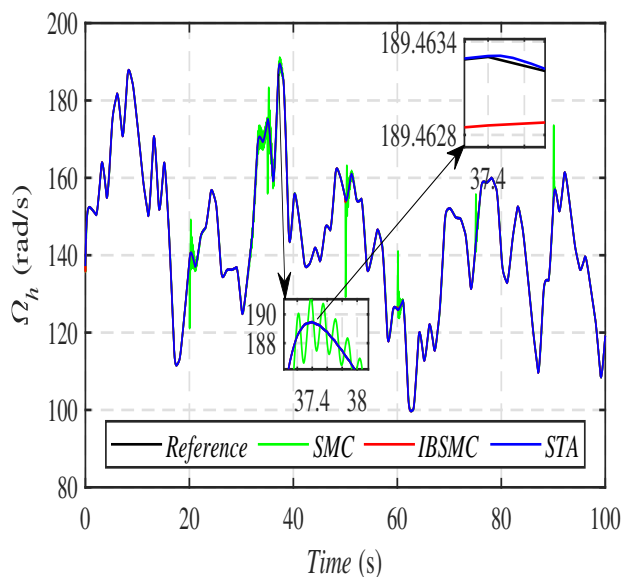


Fig. 16. Desired and actual, HSS angular speeds for case 1(b)

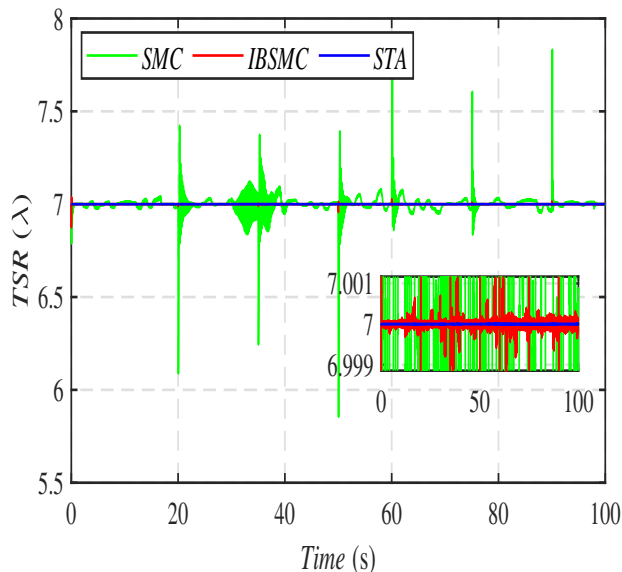


Fig. 17. TSR versus time for case 1(b)

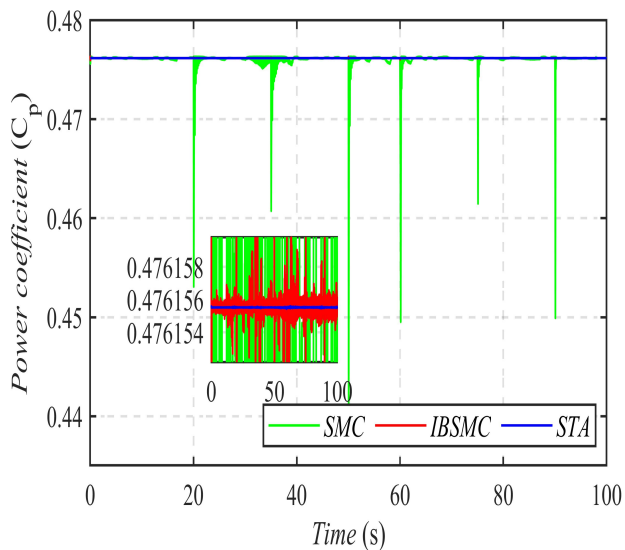


Fig. 18. Coefficient of power versus time for case 1(b)

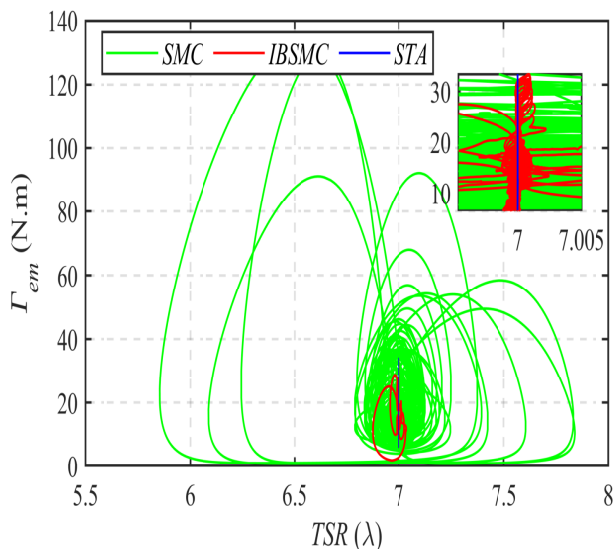


Fig. 19. TSR versus electromagnetic torque for case 1(b)

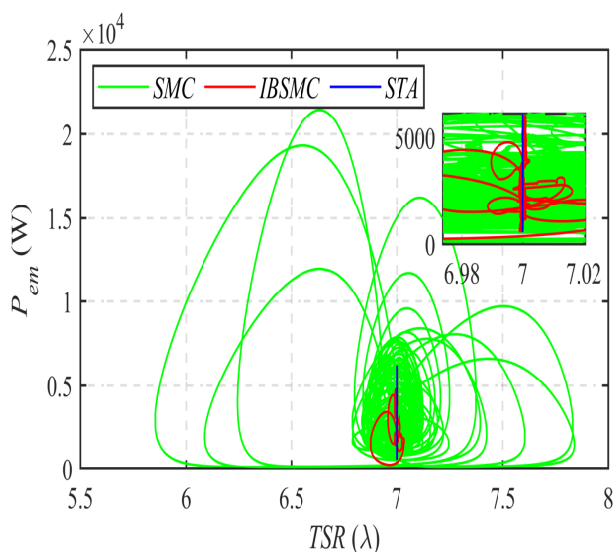


Fig. 20. Mechanical power versus TSR for case 1(b)

should operate around the optimal rotational speed for mechanical torque. Parametric variations have no effect on the STA, as demonstrated in Fig. 21.

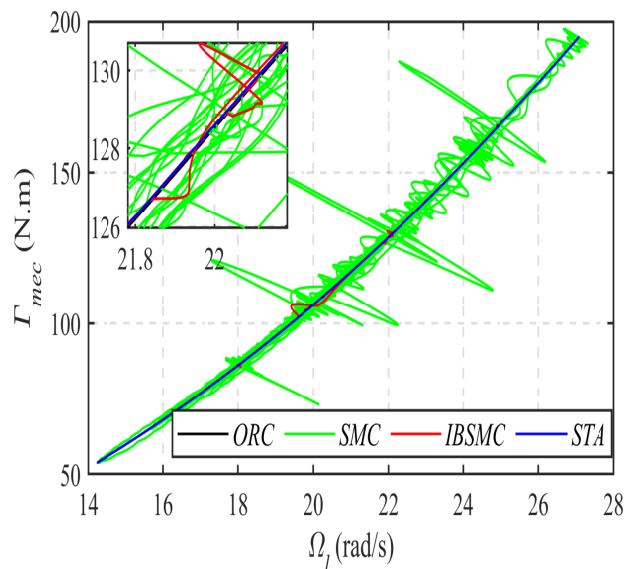


Fig. 21. Turbine shaft speed versus mechanical torque for case 1(b)

7.3. Case 2: Deterministic wind speed profile

In Fig. 22, the system ability to withstand sharp variations in wind speed is examined. This deterministic case involves sudden changes in wind speed. It is important for the system to operate at C_{pmax} when sharp variations occur. Figure 22 shows that the SMC and IBSMC experience spikes under sharp variations, while the STA maintains a smooth tracking of the reference angular speed profile of the HSS side. Although there are some transient disturbances in the power coefficient, tip speed ratio, and HSS angular speed when the wind speed is suddenly var-

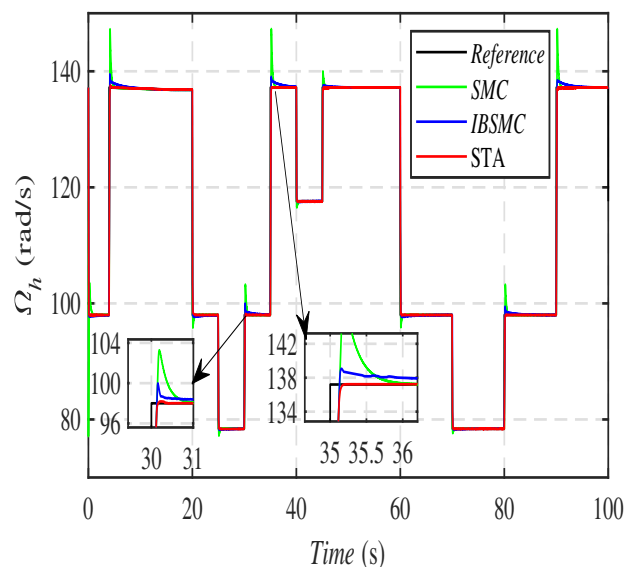


Fig. 22. Deterministic speed profile desired and actual, HSS angular speeds

ied, they do not significantly affect the stability of the control scheme or the system performance, as demonstrated in Figs. 23 and 24.

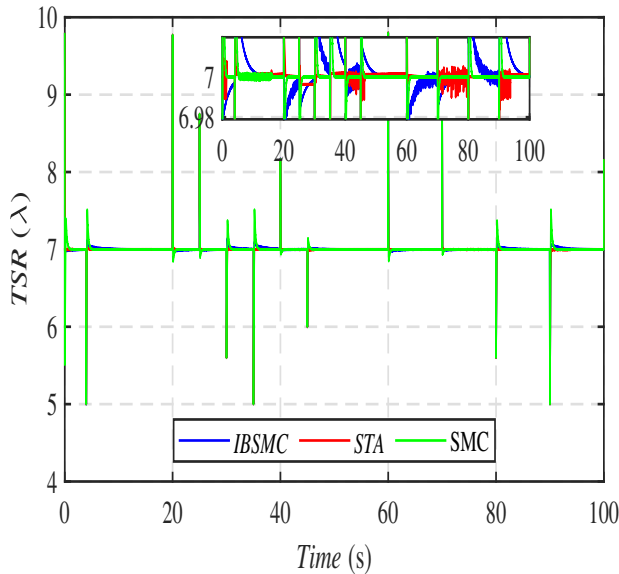


Fig. 23. TSR versus time for case 2

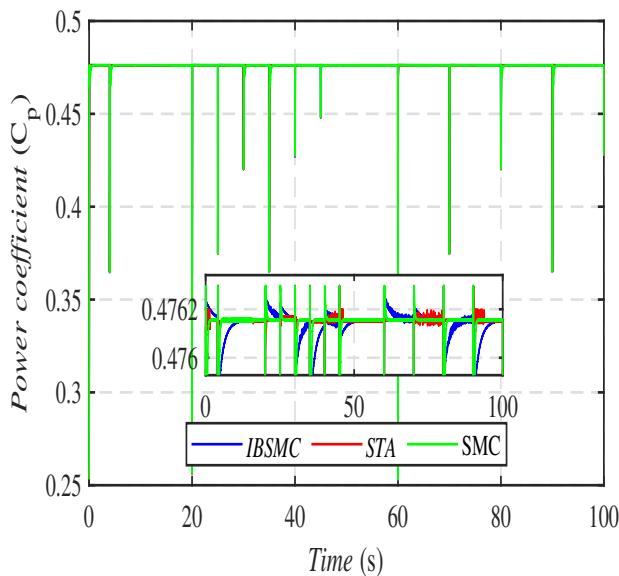


Fig. 24. Coefficient of power versus time for case 2

8. CONCLUSIONS

This research article introduces a model for PMSG-WECS. The three state model has been converted into a more simplified two-state normal form, which is output-oriented. The simplified, two-state normal form, has been subjected to act under the effect of MPPT algorithms: a conventional SMC based MPPT, an IBSMC based MPPT and STA based MPPT. The design process outlined a rigorous mathematical process for proving stability of the overall closed loop system. Moreover, all the three

MPPT algorithms have been exposed to realistic operating conditions.

- **Nominal Operating Condition:** Considering constant load and/or inertia etc.
- **Perturbed Operating Condition:** Here load and inertia have been considered to be varying.
- **Deterministic Operating Condition:** The wind speed has been considered to have a deterministic profile.

These operating tests has revealed a proof about the robustness of designed algorithms. Moreover, accessing the aerodynamic forces and especially the non-linear drift term has been a well known control challenge. The issue has been addressed by designing an off-line Function-Fitting Neural-Network (FN) for estimation of the otherwise un-accessible terms especially, $L_f^2 h(x)$ and $L_g L_f h(x)$. In addition, a High Gain Observer (HGO) has been employed to estimate the missing of High Speed Shaft (HSS) via the measurable speed of PMSG rotor. During simulation, it was noted that the STA, amongst the proposed MPPT strategies, has been proven to be more effective in terms of fast dynamic response, minimal steady-state error, smooth control actions and hence negligible chattering, and superiority in terms of robustness. The MATLAB/Simulink based tests, under stochastic and deterministic wind speed profiles authenticate the same about STA superiority.

ACKNOWLEDGEMENTS

The authors acknowledge support from the Deanship of Scientific Research, Najran University, Kingdom of Saudi Arabia, for funding this work under the Research Groups funding program grant code number (NU/RG/SERC/12/9).

The technical support from Department of Electrical Engineering, National University of Science and Technology, Islamabad, Department of Electrical Engineering, COMSATS University Abbotabad Campus, Department of Electrical, Electronics and Computer Systems of the University of Sargodha, and University of Engineering and Technology, Peshawar, Abbotabad Campus is also acknowledged.

Funding: This research was funded by the Faculty of Electrical and Computer Engineering, Cracow University of Technology and the Ministry of Science and Higher Education, Republic of Poland (grant no. E-1/2023).

REFERENCES

- [1] M.A. Abdullah, A. Yatim, C.W. Tan, and R. Saidur, "A review of maximum power point tracking algorithms for wind energy systems," *Renew. Sust. Energy Rev.*, vol. 16, no. 5, pp. 3220–3227, 2012.
- [2] S.M.R. Kazmi, H. Goto, H.-J. Guo, and O. Ichinokura, "Review and critical analysis of the research papers published till date on maximum power point tracking in wind energy conversion system," in *2010 IEEE energy conversion congress and exposition*. IEEE, 2010, pp. 4075–4082.
- [3] S. Mishra, S. Shukla, N. Verma *et al.*, "Comprehensive review on maximum power point tracking techniques: wind energy," in *2015 Communication, Control and Intelligent Systems (CCIS)*. IEEE, 2015, pp. 464–469.

Robust estimation based nonlinear HOSMC strategies for PMSG-WECS

- [4] J.S. Guimarães, B.R. de Almeida, F.L. Tofoli, and D. de Souza Oliveira, "Three-phase grid-connected wecs with mechanical power control," *IEEE Trans. Sust. Energy*, vol. 9, no. 4, pp. 1508–1517, 2018.
- [5] Q. Wang and L. Chang, "An intelligent maximum power extraction algorithm for inverter-based variable speed wind turbine systems," *IEEE Trans. Power Electron.*, vol. 19, no. 5, pp. 1242–1249, 2004.
- [6] M.A. Khan, S. Ullah, L. Khan, Q. Khan, Z.A. Khan, H. Zaman, and S. Ahmad, "Observer based higher order sliding mode control scheme for pmsg-wecs," in *2019 15th International Conference on Emerging Technologies (ICET)*. IEEE, 2019, pp. 1–6.
- [7] Z.M. Dalala, Z.U. Zahid, and J.-S. Lai, "New overall control strategy for small-scale wecs in mppt and stall regions with mode transfer control," *IEEE Trans. Energy Convers.*, vol. 28, no. 4, pp. 1082–1092, 2013.
- [8] M.A. Khan, Q. Khan, L. Khan, I. Khan, A.A. Alahmadi, and N. Ullah, "Robust differentiator-based neurofuzzy sliding mode control strategies for pmsg-wecs," *Energies*, vol. 15, no. 19, p. 7039, 2022.
- [9] C. Wei, Z. Zhang, W. Qiao, and L. Qu, "An adaptive network-based reinforcement learning method for mppt control of pmsg wind energy conversion systems," *IEEE Trans. Power Electron.*, vol. 31, no. 11, pp. 7837–7848, 2016.
- [10] S.M. Barakati, M. Kazerani, and J.D. Aplevich, "Maximum power tracking control for a wind turbine system including a matrix converter," *IEEE Trans. Energy Convers.*, vol. 24, no. 3, pp. 705–713, 2009.
- [11] M. Simoes, B.K. Bose, and R.J. Spiegel, "Design and performance evaluation of a fuzzy-logic-based variable-speed wind generation system," *IEEE Trans. Ind. Appl.*, vol. 33, no. 4, pp. 956–965, 1997.
- [12] M. Pucci and M. Cirrincione, "Neural mppt control of wind generators with induction machines without speed sensors," *IEEE Trans. Ind. Electron.*, vol. 58, no. 1, pp. 37–47, 2010.
- [13] I. Khan, A.I. Bhatti, A. Arshad, and Q. Khan, "Robustness and performance parameterization of smooth second order sliding mode control," *Int. J. Control Autom. Syst.*, vol. 14, no. 3, pp. 681–690, 2016.
- [14] I.K. Yousufzai, F. Waheed, Q. Khan, A.I. Bhatti, R. Ullah, and R. Akmeiliawati, "A linear parameter varying strategy based integral sliding mode control protocol development and its implementation on ball and beam balancer," *IEEE Access*, vol. 9, pp. 74 437–74 445, 2021.
- [15] I. Khan, "On performance based design of smooth sliding mode control," Ph.D. dissertation, 2016.
- [16] Z. Alam, I. Ahmad, S. Ullah, F. Ullah, M.A. Khan, M. Zafran, and A.U. Rehman, "Maximum power extraction from photovoltaic system using integral sliding mode control," in *2020 3rd International Conference on Computing, Mathematics and Engineering Technologies (iCoMET)*. IEEE, 2020, pp. 1–5.
- [17] I.U. Haq, Q. Khan, I. Khan, R. Akmeiliawati, K.S. Nisar, and I. Khan, "Maximum power extraction strategy for variable speed wind turbine system via neuro-adaptive generalized global sliding mode controller," *IEEE Access*, vol. 8, pp. 128 536–128 547, 2020.
- [18] Y. Soufi, S. Kahla, and M. Bechouat, "Feedback linearization control based particle swarm optimization for maximum power point tracking of wind turbine equipped by pmsg connected to the grid," *Int. J. Hydrog. Energy*, vol. 41, no. 45, pp. 20 950–20 955, 2016.
- [19] Y. Bazargan-Lari, M. Eghtesad, and B. Assadsangabi, "Study of internal dynamics stability and regulation of globular-spray mode of gmaw process via mimo feedback-linearization scheme," in *2008 International Conference on Intelligent Engineering Systems*. IEEE, 2008, pp. 31–36.
- [20] X.-Y. Lu and S. K. Spurgeon, "Output feedback stabilization of mimo non-linear systems via dynamic sliding mode," *Int. J. Robust Nonlinear Control*, vol. 9, no. 5, pp. 275–305, 1999.
- [21] I.U. Khan, L. Khan, Q. Khan, S. Ullah, U. Khan, and S. Ahmad, "Neuro-adaptive backstepping integral sliding mode control design for nonlinear wind energy conversion system," *Turk. J. Electr. Eng. Comput. Sci.*, vol. 29, no. 2, pp. 531–547, 2021.
- [22] M. Mat-Noh, M. Arshad, R. Mohd-Mokhtar, and Q. Khan, "Back-stepping integral sliding mode control (bismc) application in a nonlinear autonomous underwater glider," in *2017 IEEE 7th International Conference on Underwater System Technology: Theory and Applications (USYS)*. IEEE, 2017, pp. 1–6.
- [23] Q. Khan, A.I. Bhatti, S. Iqbal, and M. Iqbal, "Dynamic integral sliding mode for mimo uncertain nonlinear systems," *Int. J. Control Autom. Syst.*, vol. 9, no. 1, pp. 151–160, 2011.